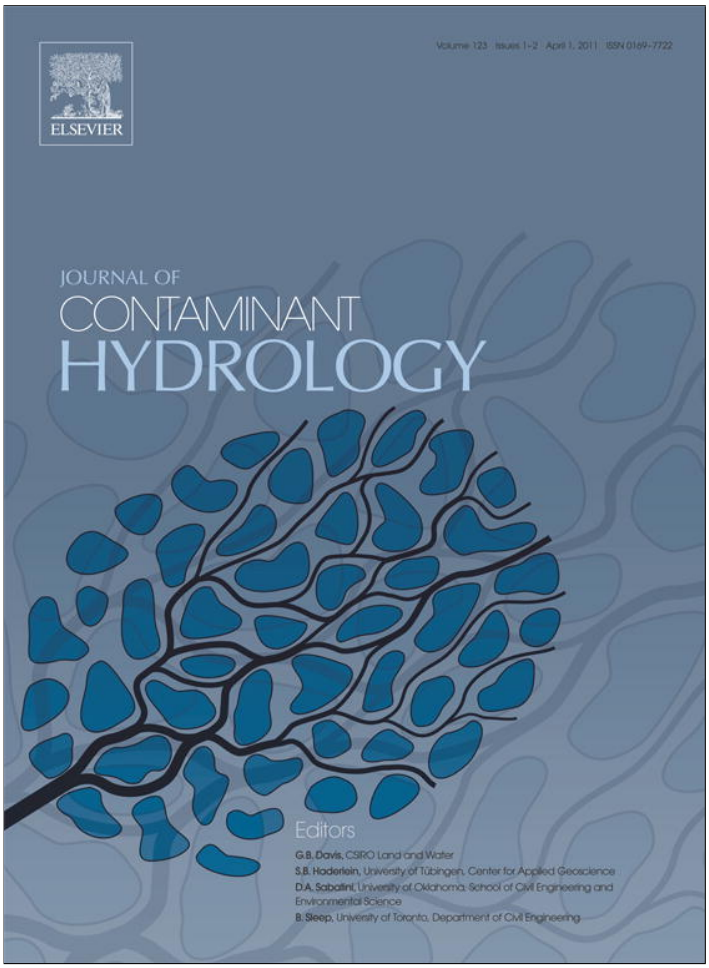

Journal of Contaminant Hydrology 123 (2011) 65–74

Contents lists available at ScienceDirect

Journal of Contaminant Hydrology

journal homepage: www.elsevier.com/locate/jconhyd

Characterization of fracture aperture field heterogeneity by electrical resistance measurement

A. Boschan [a,b,c,*], I. Ippolito [b,c], R. Chertcoff [b,c], J.P. Hulin [a,c], H. Auradou [a,c]

[a] Univ Pierre et Marie Curie-Paris 6, Univ Paris-Sud, CNRS, Lab. FAST, Bâtiment 502, Campus Paris-Sud, Orsay, F-91405 France
[b] Grupo de Medios Porosos, Departamento de Física, Facultad de Ingeniería, Universidad de Buenos Aires, Paseo Colón 850, 1063 Buenos Aires, Argentina
[c] LIA PMF-FMF (Franco-Argentinian International Associated Laboratory in the Physics and Mechanics of Fluids)

ARTICLE INFO

Article history:
Received 14 September 2010
Received in revised form 14 December 2010
Accepted 17 December 2010
Available online 30 December 2010

Keywords:
Fractures
Aperture
Heterogeneity
Channeling
Resistance
Roughness

ABSTRACT

We use electrical resistance measurements to characterize the aperture field in a rough fracture. This is done by performing displacement experiments using two miscible fluids of different electrical resistivity and monitoring the time variation of the overall fracture resistance. Two fractures have been used: their complementary rough walls are identical but have different relative shear displacements which create "channel" or "barrier" structures in the aperture field, respectively parallel or perpendicular to the mean flow velocity $\vec{U}$. In the "channel" geometry, the resistance displays an initial linear variation followed by a tail part which reflects the velocity contrast between slow and fast flow channels. In the "barrier" geometry, a change in the slope between two linear zones suggests the existence of domains of different characteristic aperture along the fracture. These variations are well reproduced analytically and numerically using simple flow models. For each geometry, we present then a data inversion procedure that allows one to extract the key features of the heterogeneity from the resistance measurement.

1. Introduction

Many important industrial processes such as nuclear or chemical waste storage or water management involve fractured media (NAS, 1996; Neretnieks, 2002; and Neretnieks et al., 1982). While the global characteristics of fracture networks are very important, modelling requires a good knowledge of their individual elements. Single fractures have often been represented as the space between two parallel plates (constant aperture field): however, numerous studies revealed that their flow and transport properties are strongly influenced by the roughness of the walls and the spatial variations of their local aperture (Keller et al., 1999; Matsuki et al., 2006; Méheust and Schmittbuhl, 2000; Nemoto et al., 2009; Oron and Berkowitz, 1998; and Watanabe et al., 2008). The determination of the geometrical and transport properties of individual fractures is therefore a key issue in view of practical applications: their heterogeneity may, for instance, lead to channeling effects.

Even though elaborate laboratory techniques have been developed to characterize the heterogeneity of porous media, few methods allow one to characterize in-situ a single fracture and predict then accurately the propagation of a contaminant. In the present paper, we demonstrate experimentally at the lab scale that electrical resistance measurements may provide such information while being adaptable to fieldscale.

In a pioneering work, Brown (1989) showed that the electrical resistance of a fracture saturated by a single conducting fluid depends on the geometrical structure of the aperture field. The electrical aperture of fractures with fractal wall surfaces was shown to be lower than that for parallel plane walls of comparable size and distance: this results from the increased tortuosity of the iso potential lines.

At the scale of a fracture network, Odling et al. (2007) demonstrated that resistance measurements may be used to

* Corresponding author. Grupo de Medios Porosos, Departamento de Física, Facultad de Ingeniería, Universidad de Buenos Aires, Paseo Colón 850, 1063 Buenos Aires, Argentina. Tel.: +54 11 43430891x235/238.
E-mail address: abosch@fi.uba.ar (A. Boschan).

0169-7722/$ – see front matter © 2010 Elsevier B.V. All rights reserved.
doi:10.1016/j.jconhyd.2010.12.007

determine the effective dispersion coefficient of a small network of fractures created in a granite plug. After saturating completely the sample by a fluid of known conductivity, they injected a second fluid of different conductivity and measured the variations of the impedance of the fracture network with time during the displacement. The longitudinal dispersion and the hydrodynamic retardation coefficients were then derived from these variations: their values were shown to depend both on the connectivity of the network and on the spatial distribution and density of the fractures.

Our objective here is to apply a similar measurement method to single rough fractures. In this latter case, previous studies performed by means of other experimental techniques have demonstrated that tracer dispersion is also largely determined by the geometrical structure of the aperture field. Bauget and Fourar (2008), and Neretnieks et al. (1982), analyzed the motion and spreading of a tracer carried by a fluid flow inside a single natural fissure in various rock samples: they observed a non Fickian dispersion even for non sorbing tracers. This behavior was accounted for by preferential flow channeling within the fracture plane.

Relative shear displacement between fracture walls may lead to localization of the flow in preferential channels, particularly for complementary rough walls with a self-affine geometry (Auradou et al., 2005; Nemoto et al., 2009; and Yeo et al., 1998). In this latter case, the mean effective hydraulic aperture depends on the relative orientation of the flow and the shear: it increases for a flow perpendicular to the shear and decreases when it is parallel to it. A statistical analysis of the aperture field demonstrated that these features are due to structural heterogeneities preferentially perpendicular to the shear.

In granite and basalt fractured samples of similar geometry, saturated by a stagnant conducting solution, electrical measurements have been reported in a radial current configuration (Plouraboué et al., 2000). These experiments demonstrated a dependence of the electrical resistance on the orientation of the relative displacement of the fracture surfaces; they also showed that, for highly conductive fluids ($\sigma_s \gtrsim 0.1$S/m), the conductivity of the fracture is controlled by that of the saturating fluid while surface conductivity is negligible. This contrasts with the studies performed in porous media where the surface conductivity cannot be neglected because of a much higher surface-to-volume ratio (Bernabé and Revil, 1995; Revil and Glover, 1998).

In the present study, the same transparent fractures as in the previous work of Boschan et al. (2009) (with roughness similar to natural granite fracture) are used to monitor the variations of the overall electrical resistance during the displacement experiments. This allows us to relate the resistance measurement to the information about the structure of the flow provided in that work by the light transmission technique.

After describing the fracture models and the experimental procedure, we report electrical resistance measurements performed during displacement at different Péclet numbers in the "channel" and "barrier" geometries. We discuss qualitatively these observations, and compare them to quantitative theoretical predictions in the simple case of parallel plates; then, two different simple models for the "channel" and "barrier" geometries are presented. The analytical and numerical predictions for these two models are then compared to the corresponding experimental results. Finally, we discuss the inversion of the resistance variation data in order to estimate fracture aperture distributions.

2. Experimental setup and procedure

2.1. Fracture models

The roughness of the fracture walls is obtained by carving plexiglas blocks by means of a computer controlled milling machine using a self-affine surface map (1360×360 points) with Hurst's exponent $\zeta = 0.8$; the geometry of such surfaces has been shown to be closely similar to that of several natural fractured rocks like granite (see Boffa et al., 1998; Bouchaud, 2003; Poon et al., 1992; and Schmittbuhl et al., 1993). Moreover, surfaces generated in this way do not display accidental large scale features (e.g. branching frequently observed in natural rocks or bending as observed on replicas). Such structures may have a large influence on the displacement process and may be difficult to separate from that of the roughness which is studied here. The length of the models is $L = 350$ mm and their width $w = 90$ mm (the length L is parallel to the mean flow which corresponds to the axis x).

The geometries of the two walls are complementary; they match perfectly when brought in contact. A normal displacement (equal to the mean aperture) is first introduced from this contact position followed by a relative shear displacement $\vec{\delta}$ of magnitude $|\vec{\delta}| = 0.75$ mm, parallel to the length L for one of the fractures and perpendicular for the other. In both cases, the mean value of the local aperture $a(x,y)$ is $<a(x,y)>_{x,y} = 0.75$ mm and its standard deviation $\sigma_{x,y}(a(x,y)) = 0.14$ mm.

Grey level maps of these aperture fields are displayed in Figs. 1 and 2. As can be seen, the shear displacement $\vec{\delta}$ introduces "heterogeneity structures" always normal to $\vec{\delta}$ (i.e. to x in the first case and to y in the second): the correlation length of the aperture is larger parallel than perpendicular to them.

When the structures are normal to the mean flow (i.e. to x), they may act as barriers (Fig. 1): one refers therefore to this case as the "barrier" geometry. Then, the average $a(x) = <a(x,y)>_y$ of the aperture in the y direction (bottom curve in Fig. 1) displays large variations with x; in contrast, the variations of $a(y) = <a(x,y)>_x$ with y are much smaller (curve at the left).

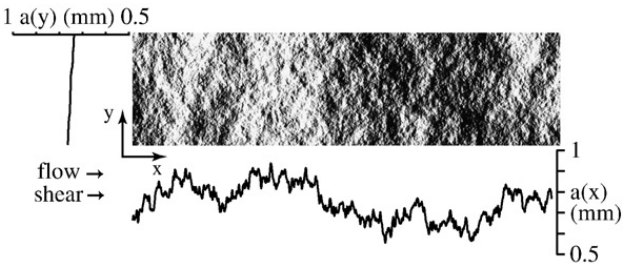

Fig. 1. Top right: grey level map of the numerical aperture field in the "barrier geometry": white = 1 mm, black = 0.5 mm. Map size: 1360 by 360 pixels. Bottom: profile of the average $a(x) = <a(x,y)>_y$ of the aperture over the width $w = 90$ mm of the model; left: profile of the average $a(y) = <a(x,y)>_x$ over the length $L = 350$ mm.

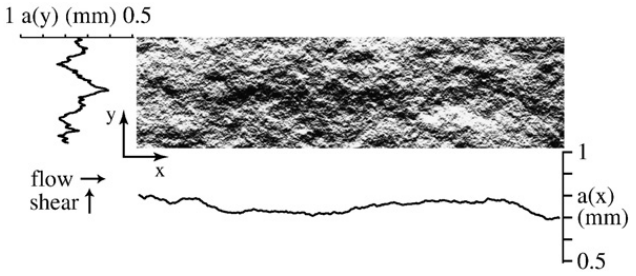

Fig. 2. Top right — grey level map of the numerical aperture in the "channel geometry": The size of the map, the grey level code and the meaning of the curves at the bottom and at the left are the same as in Fig. 2.

When the heterogeneity structures are dominantly parallel to the mean flow (and, therefore, to x), they may act as preferential channels (Fig. 2): for this reason, in the following this case is referred to as the "channel" geometry. In the map of Fig. 2, there is, for instance, a zone of low aperture half way between the lateral sides of the model and extending along most of its length. These "channels" produce large variations of the average $a(y)=<a(x,y)>_x$ with y (left curve), while $a(x)=<a(x,y)>_y$ varies much less with x (bottom curve).

2.2. Experimental set up and fluids

The fracture model is set vertically (Fig. 3). The longest vertical sides (acting as lateral borders to the flow) are sealed while the two horizontal sides are open (inlet–outlet). The upper side of the model (outlet) is connected to a syringe pump sucking the solutions upward out of the fracture. The lower horizontal side (inlet) is dipped into a fluid bath which may be moved up and down: this allows one to replace the fluids conveniently in the initial phase of the experiments. The fracture model is transparent and placed between a light panel and a Roper Coolsnap HQ CCD camera allowing for simultaneous light transmission measurements (Boschan et al., 2009).

For the electrical measurements, two stainless steel grids ($90\times20\times1\,mm^3$) used as the electrodes are placed in the inlet and outlet, and connected to a HP 4284A impedance analyzer with a measurement frequency of 1 kHz. The measurement frequency is chosen so that the reactive (imaginary) component of the impedance is very small compared to the resistive (real) one. This choice also allows one to avoid electrode polarization.

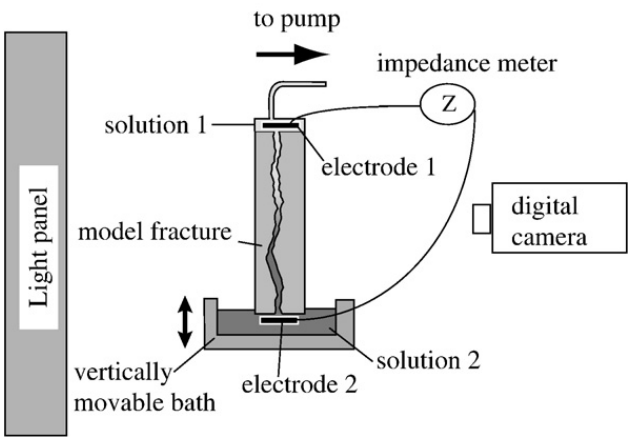

Fig. 3. Schematic view of the experimental setup.

The fluids used here are Non-Newtonian shear thinning solutions with the same concentration of scleroglucan (1000 ppm) in water. Their rheological characteristics are discussed by Boschan et al. (2009). One fluid is dyed with 0.3 g/l of Anilin Blue dye (Horobin and Kiernan, 2002) while the other contains the same amount of NaCl (as a result, the first solution is dark blue and the second transparent). This allows one to minimize buoyancy driven instabilities by matching the densities of the two solutions and also to introduce a contrast between their electrical conductivities and light transmissivities. For clarity and concision, the two solutions are referred to in the following as solution d (dye) and solution s (salt). Their respective conductivities were measured independently and are: $\sigma_s=2.27$ mS/cm and $\sigma_d=2$ mS/cm.

Polymer solutions have been selected in these experiments for two reasons. First, at high velocities, their shear thinning properties enhance the macrodispersion due to large scale heterogeneities of the flow field (Boschan et al., 2009): this macrodispersion is reflected by large structures of the displacement front which provide valuable information on the heterogeneities. Moreover, at low flow velocities, the effective viscosity of the solutions is high: this further reduces the development of unwanted buoyancy driven instabilities due to residual density contrasts.

2.3. Experimental procedure for displacement experiments

Initially the fluid bath in the bottom of the fracture is saturated with solution d while the fracture is saturated with solution s. When the pump is turned on, the flow is established and solution d displaces solution s. The electrodes allow one to measure the overall fracture electrical resistance at all times during displacement. Light transmission measurements are performed simultaneously (Boschan et al., 2009). The mean fluid velocity U ranges between 0.0024 and 0.24 mm/s (or $2.8<Pe<285$ in which the Péclet number Pe is defined by $Pe=U\langle a(x,y)\rangle_{x,y}/D_m$).

The time variation of the resistive and the reactive components of the impedance are recorded, but, due to the fact that the reactive component of the impedance is always about three orders of magnitude smaller than the resistive one, and also that a two-electrode array is not well suited for reactance measurements, we will focus exclusively on the resistance.

In the case of solution d displaced by solution s, the resistance decreases monotonously from a value corresponding to the fracture fully saturated with solution d (more resistive), down to the value corresponding to full saturation by solution s.

The ratio of the surface and bulk conductivities is characterized by the Dukhin number (Leroy et al., 2008). In the present experiments, the bulk conductivity is $\sigma_s=0.227$ S/m, leading to: $a\sigma_s=1.710^{-4}$ S ($a=0.75$ mm is the mean aperture). Assuming, from the literature, a value of order 10^{-9} S for the surface conductivity (Revil and Glover, 1998), one finds a Dukhin number of order 10^{-4}. Therefore, here, the contribution of the surface conductivity to the overall fracture resistance is very small and can be neglected.

2.4. Fracture resistance for full saturation with one or other solution

Before analyzing the displacement process, we discuss first the resistance value when the fractures are fully saturated by only one type of solution (Table 1).

In our experimental conditions the electrical resistance is expected to be proportional to the resistivity of the saturating solution. Under these assumptions, the ratio R_s/R_d of the resistivities measured for solutions s and d should be the same for the two models: the values of these ratios listed in Table 1 are indeed equal to within $\pm 2\%$ so that:

$$\frac{R_s}{R_d} = \frac{\rho_s}{\rho_d} = 0.82 \pm 0.02. \quad (1)$$

This value represents the resistivity contrast between the solutions as measured on the experimental device. The ratio of the electrical resistances measured for the two models when saturated with the same solution is also independent of the solution with:

$$\frac{R_{channel}}{R_{barrier}} = 0.85 \pm 0.03. \quad (2)$$

The values of the resistances have been compared to those predicted for a parallel plate with aperture a equal to the average $<a(x,y)>_{x,y} = 0.75\,\text{mm}$ (identical for the two models). The corresponding resistances are respectively $R_s^{pp} = L/(wa\sigma_s) = 22.8\,k\Omega$ and $R_d^{pp} = L/(wa\sigma_d) = 26\,k\Omega$ (these are calculated using the values of σ presented in Section 2.2).

The values of the ratio R/R^{pp} are listed in Table 1: it is close to one in the channel geometry and 10% higher in the barrier one. This implies that, in this latter case, the roughness has a stronger influence on the fracture resistance. The difference reflects the anisotropy of the aperture field: similar differences between two such configurations, of even larger amplitude, have been reported for the values of the permeability (Auradou et al., 2005).

These measurements confirm the linear variation of the overall fracture resistance with the electrical resistivity of the saturating fluid and suggest the use of a normalized variable in order to eliminate the influence of the particular values of σ_s and σ_d. The resistance R is then replaced in the following by R^* with:

$$R^* = \frac{R - R_d}{R_s - R_d}, \quad (3)$$

when solution d displaces the solution s and by

$$R^* = \frac{R - R_s}{R_d - R_s}, \quad (4)$$

when solution s displaces the solution d. In this way, R^* is always equal to 1 at the beginning of the experiments and to 0 at the end. In order to compare easily the experiments the time t is also replaced by the reduced variable: $t^* = Ut/L$ (where U is the mean flow velocity and L the fracture length). Note that $t^* = 1$ corresponds to an injected volume equal to the pore volume of the fracture.

Table 1
R_s, R_d, R_s/R_d: Electrical resistances and their ratio when the models are fully saturated by solutions s or d. R/R^{pp}: ratio of the measured resistance in each geometry to a parallel plate of same average aperture.

	$R_s(k\Omega)$	$R_d(k\Omega)$	R_s/R_d	R/R^{pp}
Barrier	25.5 ± 0.2	30.5 ± 0.2	0.83 ± 0.01	1.15 ± 0.03
Channel	21.5 ± 0.2	26.5 ± 0.2	0.81 ± 0.01	0.98 ± 0.04

3. Displacement experiments: results

3.1. Channel geometry

The resistance R^* decreases at first linearly with t^* with a constant slope up to $t^* \simeq 0.7$ (Fig. 4). For $t^* \geq 0.7$, one observes a tail-like variation and the slope decreases continuously to zero. R^* becomes zero only for values of t^* significantly larger than 1. This indicates that a sizable fraction of the displaced solution is located in slow flow paths and leaves the model significantly after the mean transit time ($t^* = 1$) corresponding to the injection of one pore volume. The variations of R^* with t^* at the different Péclet numbers are qualitatively similar: the slope at short times (and therefore the efficiency of the displacement) increases with Pe. At long times, the full displacement ($R^* = 0$) is obtained roughly at the same normalized time at all Pe values (i.e. $t^* \sim 1.5 - 1.7$).

3.2. Barrier geometry

In this geometry, unlike in the previous one, the full saturation by the displacing solution (i.e. $R^* = 0$) is nearly reached for $t^* = 1$ (injection of one pore volume) at all Péclet numbers and the tail-like features are barely visible (Fig. 5). This indicates that no continuous and sizable slow or fast flow paths are present.

Moreover, the slope dR^*/dt^* is not constant: it is lower than the average trend for $0 < t^* < 0.5$ and higher for $0.5 < t^* < 0.8$ (the transition is marked by the vertical dashed line in Fig. 5). Moreover, the variations of the slope with t^* are

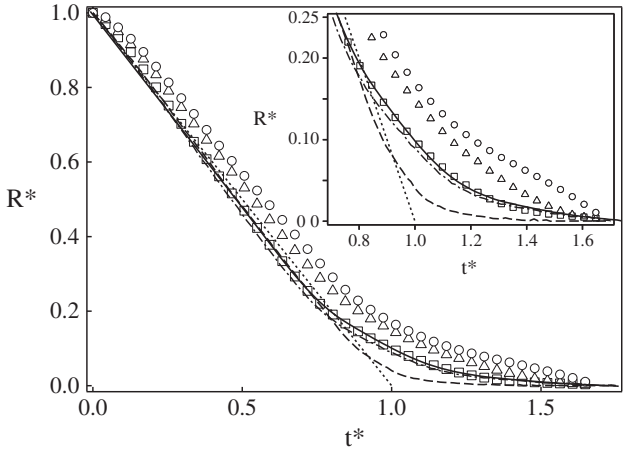

Fig. 4. Variation of the normalized resistance R (Eq. (3)) as a function of the reduced time $t = Ut/L$ in the channel geometry. Experimental data for (◦): $Pe = 28$, (△): $Pe = 142$, (□): $Pe = 285$. Dotted line: parallel plate model, solid (resp. dashed dotted) lines: predictions of analytical and numerical models from Section 4.2 for $n = 0.26$; dashed line: numerical model for $n = 1$. Inset: enlarged view of bottom right of the main graph.

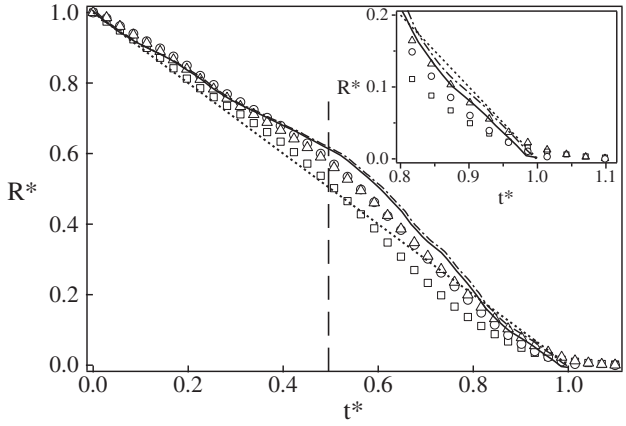

Fig. 5. Variation of the normalized resistivity R as a function of the reduced time $t = Ut/L$ in the barrier geometry. The symbols used for the experimental data are the same as in Fig. 4. Dotted line: parallel plate model (Eq. (10)), solid (resp. dashed dotted) lines: predictions of analytical and numerical models from Section 4.3. Vertical dashed line: value of t at the transition between variations of $R(t)$ with different slopes. Inset: enlarged view of bottom right part of the main graph.

significantly larger at the two lowest Péclet numbers than for $Pe = 285$.

The observations in the channel and barrier geometries and the differences between them confirm therefore that, in both configurations, the variation of R^* with t^* provides information on the structure of the flow field.

4. Displacement experiments: models

In this section, the resistance variation is modelled first in the simplest case of a parallel plate approximation and then using two different simplified representations of the flow field for the parallel and perpendicular cases.

4.1. Parallel plates geometry

The description assuming two parallel plane surfaces at a distance a provides a reference curve for determining the deviations induced by different kinds of heterogeneities. Also, this assumption will be used to evaluate the influence of the conductivity contrast between the two solutions and of the mixing zone.

Regarding this latter issue, at large enough times, the combination of advection and transverse molecular diffusion leads to a diffusive spreading regime often called Taylor dispersion (Boschan et al., 2003; Taylor, 1953). The average c_d of the concentration of solution d over the aperture satisfies then:

$$c_d(\zeta) = \frac{1}{2}(1 \pm Erf(\zeta)); \tag{5}$$

where $\zeta = (x - Ut) / \left(2\sqrt{Dt}\right)$, x is the distance from the fracture inlet, U the mean flow velocity, t the time and D the dispersion coefficient. In this equation, the plus (respectively minus) sign corresponds to the situation in which the fracture is initially saturated by solution d (respectively s).

For flow between parallel plates, the local resistivity $\rho(x,y,t)$ is constant in the y direction, so that the overall electrical resistance is related to the variation along the length L of the fracture by:

$$R(t) = \frac{1}{aw}\int_0^L \rho(x,t)dx, \tag{6}$$

in which $\rho(x,y,t) = \rho(x,t)$ is related to the local relative concentration c_d of solution d by: $1/\rho(x,t) = c_d(x,t)\sigma_d + (1 - c_d(x,t))\sigma_s$. Eq. (6) then becomes:

$$R(t) = \frac{1}{\sigma_s aw}\int_0^L \frac{1}{1-\chi c_d(x,t)}dx, \tag{7}$$

where $\chi = 1 - \sigma_d/\sigma_s$. In the assumption of a small contrast between σ_s and σ_d, one has $\chi c_d \ll 1$. Eq. (7) may then be approximated by:

$$R(t) \simeq \frac{1}{\sigma_s aw}\left(L + \chi\int_0^L c_d(x,t)dx\right). \tag{8}$$

The integral at the right is the ratio of the volume of solution d inside the fracture by the section aw transverse to the mean flow. For a fracture initially saturated by solution s, mass conservation requires that this integral be equal to Qt/aw in which Q is the volume flow rate. Then, Eq. (8) becomes:

$$R(t) \simeq \frac{1}{\sigma_s w}\left(\frac{L}{a} + \chi\frac{Q}{a^2 w}t\right). \tag{9}$$

Since the ratio $Q/(aw)$ is equal to the mean velocity U which is also that of the front, the resistance varies linearly from $R_s = L/(aw\sigma_s)$ to $R_d = L/(aw\sigma_d)$. In the other flow configuration (solution d displaced by solution s), Qt must be replaced by $awL - Qt$.

Using the normalized variables R^* and t^* defined in Section 2.4, Eq. (9) becomes:

$$R^* = 1 - t^*. \tag{10}$$

This variation is represented as a reference by a straight dotted line in Figs. 4 and 5. Due to the normalization, the slope is always negative ($= -1$) while it may be of either sign for the variation of $R(t)$.

The variation from Eq. (10) does not depend on the dispersion coefficient D; this is however only valid as long as the upstream part of the concentration variation front has not reached the end of the fracture and all the injected solution is still within it.

In order to evaluate the influence of this latter effect, as well as of the approximation made by replacing Eq. (7) by Eq. (8), Eq. (7) has been integrated directly, using Eq. (5) in order to estimate $c_d(x,t)$. The dispersion coefficients D (or equivalently the normalized dispersivities $\alpha/a = D/(Ua)$) are taken equal to the upper and lower values determined previously from the light transmission technique (Boschan et al., 2009). The result of this computation is compared in Fig. 6 to the linear variation from Eq. (10).

For example, for $\chi = 0.12$, the curves computed from Eq. (7) are, at first, only slightly below the linear variation from Eq. (10). When the forward part of the displacement front reaches the end of the model, there is an upward

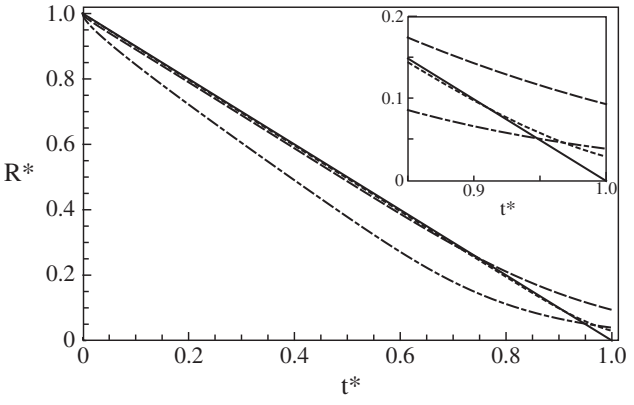

Fig. 6. Theoretical variation of the resistance with time in the parallel plate model. Solid line: prediction from Eq. (10). Dotted and dashed lines: normalized resistivity variation $R(t)$ computed by integrating Eq. (7) for $\chi=0.12$ and, respectively, $\alpha/a=1$ and $\alpha/a=10$. Dash–dotted line: variation of $R(t)$ computed for $\alpha/a=10$ and $\chi=0.7$. Inset: enlarged view of bottom right of the main graph.

curvature of the variation and R^* becomes larger than the value predicted by the parallel plate model as $t^*\to 1$ (see inset). This occurs earlier for $\alpha/a=10$ ($t^*\simeq 0.75$) than for $\alpha/a=1$ ($t^*\simeq 0.92$): this difference reflects the broader width of the front due to dispersion for $\alpha/a=10$. The value of R^* differs still significantly from 0 at $t^*=1$: this shows that the saturation of the fracture by the displacing solution is incomplete.

For the larger conductivity ratio $\chi=0.7$, the curve derived from Eq. (7) (dash–dotted line) is clearly below the linear variation predicted by Eq. (10): this implies that the first order approximation used to obtain Eq. (8) is not valid any more. Even when the deviation from the linear variation is large, none of the curves obtained for different values of α/a and χ displays abrupt slope variations comparable to those observed on the experimental curve of Fig. 5.

The above results demonstrate that the variation of the electrical resistance is mainly determined by the dynamics of the displacement front separating regions saturated by the two types of solutions. The hydrodynamic dispersion only adds a tail feature to the curves for t^* values close to 1. In the following models, χ is always taken small and the variation of the resistance are assumed to be determined exclusively by convective processes (i.e. the effect of local dispersion is neglected).

We shall now take into account the effect of the heterogeneities of the flow field by means of two different models specifically adapted to either perpendicular or parallel geometries.

4.2. Channel geometry

4.2.1. Velocity field and front displacement

In this case, the fracture is described as a set of independent channels parallel to the mean flow (see Fig. 7 left) and of aperture $a(y)$ constant with x (a previous study (Boschan et al., 2009), has indeed shown that this model reproduces well the large scale geometry of the displacement front. As in Fig. 2, $a(y)$ is equal to the average $<a(x,y)>_x$.

In order to compute explicitly the profile of the front separating the two fluids, the polymer solutions used in the

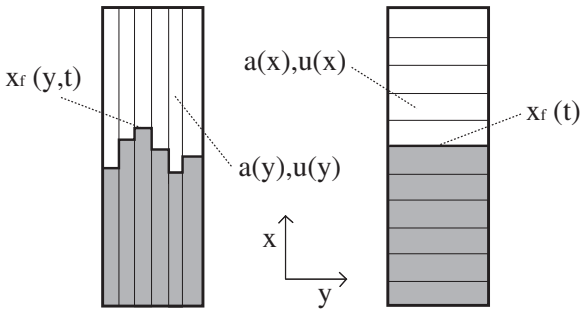

Fig. 7. Schematic view of the front geometry with the aperture and velocity distributions for the channel (left) and barrier (right) models. Grey (white) zones: portions of the fracture saturated with the displacing (respectively displaced) solution). Channels and barriers are represented for simplicity as discretized objects but the aperture $a(y)$(resp. $a(x)$) and the velocity $u(y)$(resp. $u(x)$) are actually continuous functions.

present experiments are assumed to be power law shear thinning fluids of rheological exponent n at the highest Péclet numbers (the effective viscosity μ is related to the shear rate $\dot{\gamma}$ by : $\mu\propto\dot{\gamma}^{-n}$). The value $n=0.26$ has been obtained by means of independent rheological measurements (see Boschan et al., 2009). The velocity $u(y)$ is then:

$$u(y)=\frac{\overline{u}a(y)^{(n+1)/n}}{\langle a(y)^{(n+1)/n}\rangle_y}, \tag{11}$$

in which $\overline{u}=\langle u(y)\rangle_y$ is the mean fluid velocity (in x) across the fracture. The front profile $x_f(y,t)$ is then given by:

$$x_f(y,t)=u(y)t. \tag{12}$$

The resulting profiles display large structures with an amplitude increasing linearly with time (Boschan et al., 2009).

At low *Pe* values (low velocities), the solutions behave like Newtonian fluids with $\mu=cst.$, corresponding to $n=1$.

4.2.2. Analytical computation of the resistance

Since local dispersion is neglected, each local fluid element of the fracture is assumed to be composed by only one type of solution: the displacement front is therefore the boundary between the two regions occupied by each type of solution.

If we assume that there is no transverse transport of electrical current, then, Eq. (7) can be applied to each elementary channel by replacing a by its local value $a(y)$ and taking into account the variation of $c_d(y,t)$ with y. The elementary channels are in parallel so that their conductances add up. Using again a first order approximation with respect to $\chi\ll 1$ provides the following expression of the overall effective conductance:

$$\frac{1}{R(t)}=\frac{\sigma_s}{L}\int_0^w a(y)\left(1-\frac{\chi}{L}\int_0^L c_d(x,y,t)dx\right)dy. \tag{13}$$

For an elementary channel at a distance y, the integral of c_d with respect to x is either equal to L if the front

has reached the end of the model ($u(y)t \geq L$) or to $u(y)t$ otherwise ($u(y)t \leq L$). Therefore:

$$\frac{1}{R(t)} = \frac{\sigma_s}{L}\int_{u(y)t\leq L} a(y)\left(1-\frac{\chi}{L}u(y)t\right)dy + \frac{\sigma_s}{L}\int_{u(y)t\geq L} a(y)(1-\chi)dy. \tag{14}$$

At early times such that $u(y)t \leq L$ for all y, $1/R$ varies linearly with t with:

$$\frac{1}{R(t)} = \frac{\sigma_s}{L}\int_0^w a(y)dy - \frac{\sigma_s \chi t}{L^2}\int_0^w a(y)u(y)dy. \tag{15}$$

Using again a first order approximation for $\chi \ll 1$, Eq. (15) may be rewritten in the following form equivalent to Eq. (9):

$$R(t) = \frac{L}{\sigma_s \int_0^w a(y)dy}\left[1 + \frac{\chi t}{L}\frac{\int_0^w a(y)u(y)dy}{\int_0^w a(y)dy}\right]. \tag{16}$$

This expression becomes identical to Eq. (10) for R^* defined from Eq. (3) and t^* taken equal to Ut/L (U is here the arithmetic mean $\int_0^L a(y)u(y)dy / \int_0^L a(y)dy$).

This initial linear regime is left for $t_1 = L/U_M$ (i.e. $t_1{}^* = U/U_M \leq 1$) in which U_M is the maximum of the velocities $u(y)$.

At longer times, the full Eq. (14) must be used. Then, the value: $R_\infty \simeq (1+\chi)R(0)$ of the resistance corresponding to a full saturation by the displacing solution is reached at $t_2{}^* = U/U_m \geq 1$ (U_m is the minimum velocity).

The result of the computation for $n = 0.26$ (corresponding to the solutions used in the experiments) is plotted in Fig. 4 as a solid line. The predicted variation corresponds well to the experiments, particularly for $Pe = 285$: in this case, the experimental and theoretical curves coincide precisely in both the linear and in the tail of the curves.

At lower Péclet numbers, the absolute value of the slope becomes lower: this may be due to the transverse diffusion of fluid between the fastest flow paths and the slower ones.

Replacing the power law fluid by a Newtonian one (dashed line in Fig. 4) strongly reduces the tail effect: the linear variation is retained during a longer time t^* than for the shear thinning solution. This reflects the lower value of the velocity contrasts between the fast and slow paths for the Newtonian solution ($n = 1$) than for $n = 0.26$. The slope of the linear variation is however the same. The reduced value of the experimental slope at lower Pe's is therefore not accounted for by the vicinity of a Newtonian plateau of the rheological curve at lower shear rates.

4.2.3. Numerical 2D computation of the resistance

In the above model, transverse electrical transport in the y direction is neglected. It will however be present since the aperture field $a(x,y)$ is bidimensional even though it is strongly anisotropic.

In order to estimate its influence, numerical simulations have been performed: the full *2D* aperture field $a(x,y)$ is used for computing the electrical resistance while, at all times, the front $x_f(y,t)$ is computed in the same way as above. The fractured is modelled as a two dimensional array of resistors with mesh sizes δl and δw respectively along x and y. The resistance of a node of coordinates (x,y) is taken equal to:

$$r(x,y) = \frac{\delta l}{\sigma a(x,y)\delta w}, \tag{17}$$

in which σ is equal to σ_s or σ_d depending on the type of solution saturating the node.

The array is considered as a set of bonds linking two nodes of the array and with a resistance equal to the mean of that of the nodes. At each time step, the computation of the equivalent resistance by writing Ohm's law for every bond leads to a set of linear equations solved by means of a conjugate gradient method. Like for the analytical model, the predicted variation of $R^*(t^*)$ with t^* is independent of Pe (local dispersion and molecular diffusion are again neglected).

The variation $R^*(t^*)$ obtained in this way is represented by a dashed–dotted line in Fig. 4. The values obtained are very similar to the predictions of the simpler analytical model (solid line). This shows that the transverse electrical currents have almost no influence on the electrical resistance, at least in the channel geometry. This justifies therefore the use of the analytical model in the inversion tests discussed below.

4.3. Barrier geometry

4.3.1. Velocity field and front displacement

In this geometry, corresponding to the aperture field of Fig. 1, we assume that the front between the two solutions remains flat at all times; however, its velocity $dx_f/dt = u(x)$ varies with distance so that the flow rate $Q = u(x)a(x)w$ remains constant while the mean aperture $a(x)$ varies (see Fig. 7 right). The transit time $t(x_f)$ of the front from $x = 0$ to $x = x_f$ is:

$$t = \int_0^{x_f}\frac{dx}{u(x)} = \frac{w}{Q}\int_0^{x_f} a(x)dx. \tag{18}$$

In contrast with the channel geometry, this relation does not depend on the rheology of the fluid (the latter influences only the local velocity profile between the walls of the fracture and is therefore not relevant in the present model).

4.3.2. Analytical and numerical computation of the resistance

In this barrier geometry, the overall effective resistance is obtained by summing the resistances of the slices corresponding to different distance x and which are, this time, in series. In the case in which solution s is displaced by solution d, this leads to:

$$R(t) = \frac{1}{\sigma_s w}\left(\int_0^L \frac{dx}{a(x)} + \chi\int_0^{x_f(t)}\frac{dx}{a(x)}\right). \tag{19}$$

The slope dR/dt of the variation is not constant with time like in the case of the parallel plates but is given by:

$$\frac{dR(t)}{dt} = \frac{\chi}{\sigma_s w^2}\frac{Q}{a^2\left(x_f(t)\right)}, \tag{20}$$

in which $Q = a(x_f(t))w\,dx_f/dt$ is (as above) the flow rate.

Eq. (19) may be rewritten using the dimensionless variables R^* defined by Eq. (3) and t^* defined by:

$$t^* = \frac{t\left(x_f\right)}{t(L)} = \frac{\int_0^{x_f} a(x)dx}{\int_0^L a(x)dx} = \frac{Ut}{L}, \tag{21}$$

in which U is the harmonic mean of the velocities $u(x)$ over the distance L. The variation of R^* as a function of t^* is plotted in Fig. 5 as a solid line and does not depend on Pe.

In contrast with the channel geometry, no tail is observed, but the slope varies significantly during the displacement: from Eq. (20), this reflects the variations of the aperture $a(x)$. Quantitatively, the values obtained are in better agreement with the experimental data (symbols) for experiments corresponding to the two lowest Péclet numbers ($Pe=28$ and $Pe=142$). This may reflect the increase of the longitudinal dispersion at high flow rates.

Like in the channel geometry, the influence of transverse electrical current on the value of the resistance is verified by computing the electrical resistance by means of a *2D* numerical computation based on the full aperture $a(x,y)$. In contrast, the front is still assumed to be flat and its displacement is computed as above. The numerical procedure for computing the resistance at a given time is the same as for the channel geometry and the result is plotted in Fig. 5 as a dashed–dotted line.

The values are again very similar to those predicted by the simpler analytical model which is therefore always used for computing the electrical resistance in the inversion procedures below. The results reported here demonstrate that the deviations from the linear resistance variation (parallel-plate model) induced by barrier or channel structures are of very different kinds which may be critical in order to characterize the heterogeneity. We demonstrate now that the resistance measurement may be used to obtain quantitative information on the fracture heterogeneity (this represents indeed a key issue in view of practical applications).

5. Inversion of experimental resistance variation data

Two different approaches are used in this section depending on the features of the variation of the resistance with time. Practically, we seek to determine from this variation the parameters of the simplified theoretical description from Section 4.2 or 4.3 suitable for the case considered.

5.1. Inversion of the data for the channel geometry

In this case, the resistance displays a roughly linear variation followed by a tail. Most of the information on the distribution of the apertures and flow velocities is provided by the tail: it corresponds to the transition between the breakthrough of the front at the end of the model ($x=L$) in the fastest channels and in the slowest ones. This is clearly seen by differentiating Eq. (14) with respect to time. Only the first integral contributes to the derivative since the second corresponds to channels already fully saturated with the displacing solution. This leads to:

$$\frac{d}{dt}\left(\frac{1}{R(t)}\right) = -\frac{\sigma_s \chi}{L^2}\int_{u(y)t\le L} a(y)u(y)dy. \tag{22}$$

The variation of $d(1/R)/dt$ with time is plotted in Fig. 8a. The Péclet number $Pe=285$ has been selected because it corresponds to the best fit of the theoretical models with the experimental variation. After a transient initial rising part, a plateau value is reached (dashed line) and, then, the slope decreases in the tail part of the curve $R(t)$ (here for $t\ge 800$ s): in the following, this will be the range of times of interest. The initial rise likely corresponds to the time required for the homogeneization of the distribution of the fluids over the distance between the fracture walls after the initial injection.

Actually, the integral in Eq. (22) represents the cumulative flow rate $Q(u_c)=\int_0^{u_c} q(u)du$ in the channels of velocity u (y) $\le u_c = L/t$: at short times, this condition is met for all channels and $Q(u_c)=Q$. The derivative $q(u)=dQ/du$ characterizes therefore the distribution of the flow in the model between the channels of different velocities. Derivating Eq. (22) with respect to time leads to:

$$\frac{d^2}{dt^2}\left(\frac{1}{R(t)}\right) = -\frac{\sigma_s \chi}{L^2}\frac{du}{dt}q(u), \tag{23}$$

with $u=L/t$ so that, replacing du/dt as a function of t,

$$t^2\frac{d^2}{dt^2}\left(\frac{1}{R(t)}\right) = \frac{\sigma_s \chi}{L}q(u). \tag{24}$$

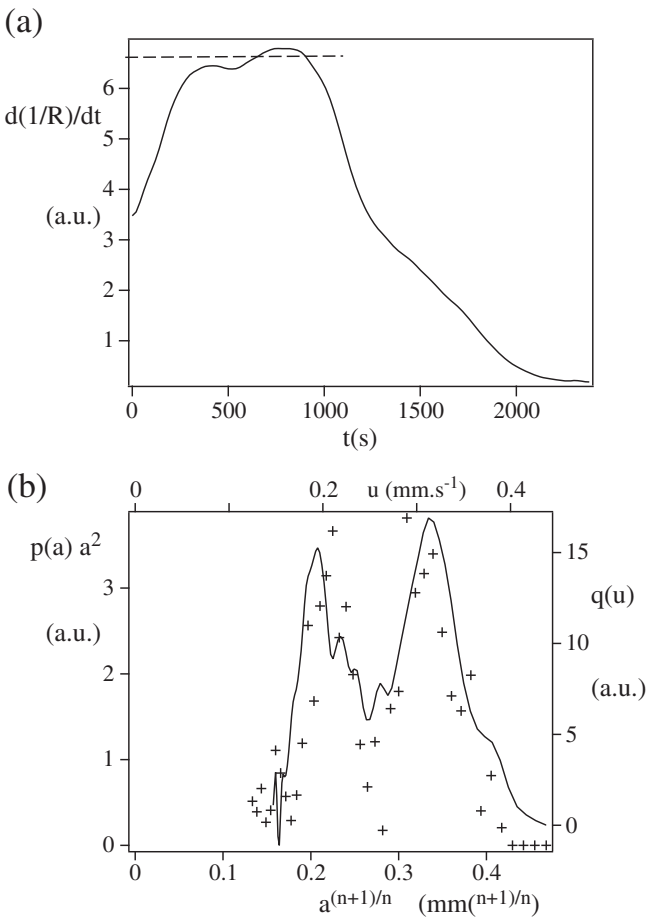

Fig. 8. Data inversion for the channel geometry. a) Variation of the derivative $d/dt(1/R)$ as a function of time for the experiment at $Pe=285$ in the channel geometry. b) Compared variations of the distribution $q(u)$ of the flow rate as a function of the velocity u for the same experiment (solid line) and of $p(a)a^2$ as a function of $a^{(n+1)/n}$ (crosses).

The distribution $q(u)$ for values of u such that the corresponding time L/u is in the tail region is displayed in Fig. 8b.

The function $q(u)$ may then be related to the normalized probability distribution $p(a)$ of the apertures of the channels. This distribution $p(a)$ has been determined from the mean aperture profile $a(y)$ (see Fig. 2). The function $q(a)$ is then given by $q(a) = wau(a)p(a)$ and related to $q(u)$ by $q(u) = q(a)da/du$. Also, from Eq. (11), the velocity $u(a)$ in a region of local aperture a is proportional to $a^{(n+1)/n}$. Combining these relations leads to $q(u) \propto a(u)^2 p(a(u))$ (the order of magnitude of the proportionality coefficient may be roughly estimated but its precise value depends on the geometry of the rough surfaces). These two estimations of $q(u)$ are compared in Fig. 8; the scales have been adjusted and the variable $a^{(n+1)/n}$ is used for the horizontal (upper) axis in order to make the comparison easier.

Both distributions have a double peaked shape and the values of ratio between the values of u corresponding to these peaks are also similar. This confirms that information on the flow probability distributions can be obtained from the resistance variation curves. Obtaining information on the spatial distribution of the flow (particularly in the direction y) is however of course not possible for this measurement configuration. Local sensors with some spatial resolution in the direction y would be useful for that purpose.

5.2. Inversion of the data for the barrier geometry

In this configuration in which heterogeneities are barriers perpendicular to the mean flow, the variation of the resistance with time allows one to determine the longitudinal aperture profile $a(x)$. Assuming that the aperture has a value $a(x)$ independent of the transverse distance y, Eq. (20) predicts indeed that $dR(t)/dt \propto 1/a(x)^2$. This relation is applicable if local dispersion is negligible: practically, the width of the front must remain small compared to the characteristic distances of variation of the aperture along x.

The different factors in the proportionality relation between $dR(t)/dt$ and $1/a(x)^2$ in Eq. (20) are known or can be determined through independent measurements or deduced from the curves; the coefficient χ is in particular equal to $(1 - R_s/R_d)$ which, using Eq. (1), leads to the value $\chi = 0.18$. This allows one to determine $a(x_f(t))$ from $dR(t)/dt$ at any given time t: the corresponding distance $x = x_f(t)$ is then estimated by assuming for simplicity that x_f varies linearly with t. The profile $a(x)$ obtained in this way for the Péclet number $Pe = 142$ is plotted in Fig. 9 as square symbols. It is compared in the figure to the profile determined directly from the numerical aperture field. One observes that the location and amplitude of the large and medium scale structures coincide very well in the two curves. Moreover, the agreement between the absolute values of the aperture is always better than 10%.

These results show that, in the "barrier" configuration, quantitative information on the variation $a(x)$ of the mean aperture is readily obtained from the variation of the resistance with time through a simple derivation.

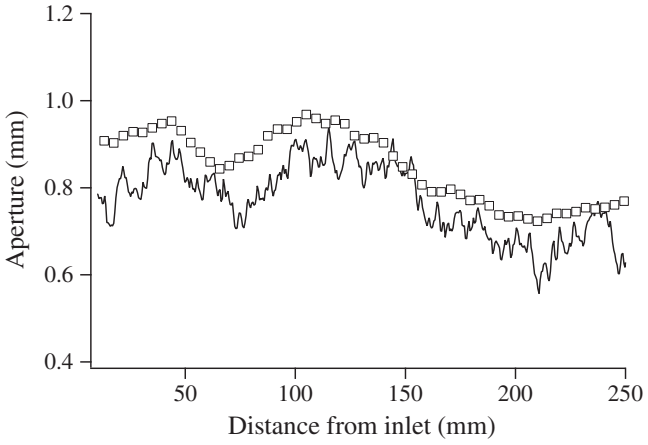

Fig. 9. Data inversion for the barrier geometry. Continuous line: longitudinal aperture profile $a(x)$ computed from the numerical aperture field (bottom graph in Fig. 1); square symbols: aperture determined from the derivative $dR(t)/dt$ using Eq. (20) ($Pe = 142, Q = 0.5$ ml/mn).

6. Discussion and conclusions

The experimental results reported here demonstrate that the variation of the overall electrical resistance with time during a miscible displacement experiment provides quantitative information about the local velocity and aperture in rough fractures at the large and medium spatial scale.

We have shown that, in order to make the interpretation simpler, the contrast between the electrical conductivities of the two solutions must be moderate.

Practically, information on the heterogeneity is provided by the nature of the deviation of the resistance variation from that for a parallel plate system of same effective aperture.

Preferential channels parallel to the mean flow (channel geometry) lead to deviations from the parallel plate variation due to early breakthrough at the outlet of the fracture; slow channels delay instead the full saturation of the medium. The velocity contrasts between these different channels as well as the distribution of the apertures may be estimated from the values of these early and late arrival times.

Barrier type features extending over a large fraction of (or all) the fracture width induce deviations of the derivative dR/dt of the variation of the resistance with time from its average value: the variations of this derivative were shown to vary as the inverse of the square of the local aperture (at least for large and medium scale variations).

It has been verified that using shear thinning fluids enhances the velocity contrasts between the different flow channels and may help detecting the heterogeneities (for example by increasing the tail effect for the channel geometry).

Local dispersion and/or heterogeneities also influence the variation of the resistance, particularly when the front width is not negligible compared to the length of the sample. Deviations associated to the longitudinal dispersion take then place mostly when the displacement front leaves the fracture. Transverse dispersion is also observed to influence the resistance: it reduces for instance the derivative of its variation with respect to time: such effects may be used to characterize this process.

In the present work, this method has only been applied to anisotropic barrier and channel-like heterogeneities: such structures can be first identified from the features of the variation of the resistance with time even if no previous knowledge of their presence is available. Then, their characteristics can be determined quantitatively by means of the

adequate inversion procedure as described in Section 5. Further studies should evaluate whether this method can be extended to different types of heterogeneities (or a combination of them): it is not clear, for instance, whether useful information can be obtained in the case of isotropic heterogeneities.

The measurements described in the present paper are applicable to natural fractured rocks like those encountered in the granitic field sites used previously for hydromechanical experiments (Cornet et al., 2003). In such cases the surface conductivity of the rocks (due for instance to clay or quartz minerals Revil and Glover, 1998) often needs to be taken into account (Ruffet et al., 1995): the analysis of the frequency dependence of the real and imaginary parts of the impedance may then provide useful complementary information. Such methods have been successfully used to characterize saturated porous media and may also be applied in the future to study the influence of the roughness of fracture walls (Leroy et al., 2008). In the case of fractured porous rocks, retardation effects due to solute exchange between the pores and the fracture must also be taken in consideration. Finally, additional information may be obtained by using several local electrodes at the inlet and outlet of the sample in order to achieve some lateral resolution in the direction transverse to the flow.

Acknowledgments

We are indebted to A. Aubertin and R. Pidoux for their assistance. H. A. and J. P. H. are supported by CNRS through GdR 2990 and by the European Hot Dry Rock Association. This work was greatly facilitated by the CNRS-Conicet International Associated Laboratory LIA-PMF (Physics and Mechanics of Fluids) and the cooperation agreement n^o 22815, the “Triangle de la Physique” RTRA Program and by the UBACYT I044 program.

References

Auradou, H., Drazer, G., Hulin, J.P., Koplik, J., 2005. Permeability anisotropy induced by the shear displacement of rough fracture walls. Water Resour. Res. 41, W09423.

Bauget, F., Fourar, M., 2008. Non-Fickian dispersion in a single fracture. J. Contam. Hydrol. 100, 137–148.

Bernabé, Y., Revil, A., 1995. Pore-scale heterogeneity, energy dissipation and the transport properties of rocks. Geophys. Res. Lett. 22 (12), 1529–1532.

Boffa, J.M., Allain, C., Hulin, J.P., 1998. Experimental analysis of fracture rugosity in granular and compact rocks. Eur. Phys. J. Appl. Phys. 2, 281–289.

Boschan, A., Charette, J., Gabbanelli, S., Ippolito, I., Chertcoff, R., 2003. Tracer dispersion of non-newtonian fluids in a Hele Shaw cell. Physica A 327, 49–53.

Boschan, A., Auradou, H., Ippolito, I., Chertcoff, R., Hulin, J.P., 2009. Experimental evidence of the anisotropy of tracer dispersion in rough fractures with sheared walls. Water Resour. Res. 45, W03201.

Bouchaud, E., 2003. The morphology of fracture surfaces: a tool for understanding crack propagation in complex materials. Surf. Rev. Lett. 10, 797–814.

Brown, S.R., 1989. Transport of fluid and electric current through a single fracture. J. Geophys. Res. 94, 9429–9438.

Cornet, F.H., Li, L., Hulin, J.-P., Ippolito, I., Kurowski, P., 2003. The hydromechanical behaviour of a fracture: an in situ experimental case study. Int. J. Rock Mech. Min. Sci. 40, 1257–1270.

Horobin, R.W., Kiernan, J.A. (Eds.), 2002. Conn's Biological Stains: A Handbook of Dyes, Stains and Fluorochromes for Use in Biology and Medicine. 10th ed. BIOS Scientific Publishers Ltd.

Keller, A., Roberts, P.V., Blunt, M.J., 1999. Effect of fracture aperture variations on the dispersion of contaminants. Water Resour. Res. 35, 55–63.

Leroy, Ph., Revil, A., Kemna, A., Cosenza, Ph., Ghorbani, A., 2008. Complex conductivity of water-saturated packs of glass beads. J. Colloid Interface Sci. 321, 103–117.

Matsuki, K., Chida, Y., Sakaguchi, K., Glover, P.W.J., 2006. Size effect on aperture and permeability of a fracture as estimated in large synthetic fractures. Int. J. Rock Mech. Min. Sci. 43, 726–755.

Méheust, Y., Schmittbuhl, J., 2000. Flow enhancement of a rough fracture. Geophys. Res. Lett. 27 (18), 2989–2992.

NAS Committee on Fracture Characterization and Fluid Flow, 1996. Rock Fractures and Fluid Flow: Contemporary Understanding and Applications. National Academy Press, Washington, D.C.

Nemoto, K., Watanabe, N., Hirano, N., Tsuchiya, N., 2009. Direct measurement of contact area and stress dependence of anisotropic flow through rock fracture with heterogeneous aperture distribution. Earth Planet. Sci. Lett. 281, 81–87.

Neretnieks, I., 2002. A stochastic multi-channel model for solute transport. Analysis of tracer tests in fractured rock. Water Resour. Res. 55, 175–211.

Neretnieks, I., Erksen, T., Tahtinen, P., 1982. Tracer movement in a single fissure in granitic rock: some experimental results and their interpretation. Water Resour. Res. 18, 849–858.

Odling, N.W.A., Elphick, S.C., Meredith, P., Main, I., Ngwenya, B.T., 2007. Laboratory measurements of hydrodynamic saline dispersion within a micro-fracture network induced in a granite. Earth Planet. Sci. Lett. 260, 407–418.

Oron, A.P., Berkowitz, B., 1998. Flow in rock fractures: the local cubic law assumption reexamined. Water Resour. Res. 34, 2811–2825.

Plouraboué, F., Kurowski, P., Boffa, J.-M., Hulin, J.P., Roux, S., 2000. Experimental study of the transport properties of rough self-affine fractures. J. Contam. Hydrol. 46, 295–318.

Poon, C., Sayles, R., Jones, T., 1992. Surface measurement and fractal characterization of naturally fractured rocks. J. Phys. D Appl. Phys. 25, 1269–1275.

Revil, A., Glover, P.W.J., 1998. Nature of surface electrical conductivity in natural sands, sandstones, and clays. Geophys. Res. Lett. 25 (5), 691–694.

Ruffet, C., Darot, M., Gueguen, Y., 1995. Surface conductivity in rocks — a review. Surv. Geophys. 16, 83–105.

Schmittbuhl, J., Gentier, S., Roux, S., 1993. Field measurements of the roughness of fault surfaces. A Review. Geophys. Res. Lett. 20 (8), 639–641.

Taylor, G.I., 1953. Dispersion of soluble matter in solvent flowing slowly through a tube. Proc. R. Soc. A. 219, 186–203.

Watanabe, N., Hirano, N., Tsuchiya, N., 2008. Determination of aperture structure and fluid flow in a rock fracture by high-resolution numerical modeling on the basis of a flow-through experiment under confining pressure. Water Resour. Res. 44 W06412.

Yeo, I.W., De Freitas, M.H., Zimmerman, R.W., 1998. Effect of shear displacement on the aperture and permeability of a rock fracture. Int. J. Rock Mech. Min. Sci. 35, 1051–1070.